Chapter 2
LSP Numerical Simulation

Abstract This chapter gives a comprehensive review on numerical simulation which could resolve engineering problems and physical problems even the nature phenomena by numerical calculation and image displayed method. At present, the main method of numerical simulation is the finite element (FE) method, the finite difference method, and the finite volume method. Compared with traditional experiment method, numerical simulation has been widely used in many fields, such as mechanical process, large building fire temperature field, and hydrogeology. Simulation methods are introduced in this chapter. For instance, the residual stress induced by laser shock processing (LSP) and the thermal relaxation behaviors of residual stress in Ni-based alloy GH4169 were investigated by means of three-dimensional nonlinear FE analysis. Fracture analysis software and crack growth model have found the application in FE analysis.

2.1 Introduction

At present, the main method of numerical simulation is the finite element (FE) method, the finite difference method, and the finite volume method. The FE method divides the continuous domain decomposition field into a finite number of units, consisting of discrete model, and then finds its approximate numerical solution. The finite difference method establishes a set of differential equations taken the place by difference to cover the space and time with the grid for approximate numerical solution. The finite volume method transforms differential equations into integral form in a physical space and scatters it. After theoretical analysis and scientific experiments, numerical simulation has become one of the main means of science and technology development.

Numerical simulation is also called computational simulation which could resolve engineering problems and physical problems, even the nature phenomena, by numerical calculation and image displayed method. Compared with traditional experiment method, numerical simulation has been widely used in many fields,

X. Ren, *Laser Shocking Nano-Crystallization and High-Temperature Modification Technology*, DOI 10.1007/978-3-662-46444-1_2

such as mechanical process, large building fire temperature field, and hydrogeology. The experimental results can be predicted by simulating the process of actual reaction with appropriated numerical simulation software, greatly saving time and manpower consumption. LSP is that the laser of high power and short pulse radiates metal surface in order that the coat of it gasifies to the high-temperature and high-pressure plasma. Compared with traditional surface strengthening, LSP possesses the advantages of no mold, easily controlling, highly flexible processing, and good surface properties after strengthening and no pollution. Therefore, it is impossible to study LSP process only relying on experiment. Numerical simulation as a kind of supplementary tool will accelerate the development and application of LSP in mechanical engineering.

2.2 A Finite Element Analysis of Thermal Relaxation of Residual Stress in Laser Shock Processing Ni-based Alloy GH4169

Abstract The residual stress induced by LSP and the thermal relaxation behaviors of residual stress in Ni-based alloy GH4169 were investigated by means of three-dimensional nonlinear FE analysis. To study the effect of different given exposure time and different temperatures on residual stress in LSP Ni-based alloy GH4169, Johnson–Cook material model was used in order to account for the nonlinear constitutive behavior. The influence of heating temperature and exposure time on the stress thermal relaxation was studied. It was concluded that stress relaxation mainly occurred during the initial period of exposure, and the degree of relaxation increased as the temperature risen. The results would provide a theoretical basis for controlling the LSP and guiding subsequent experiments.

2.2.1 Introduction

Ni-based alloy, such as GH4169, is widely used in high serving temperature fields such as space navigation, nuclear energy, and petroleum industry due to excellent fatigue resistance, radiation resistance, corrosion resistance, good machinability, and welding performance. Various mechanical surface treatment technologies, such as shot peening [1], low plastic polishing [2], and LSP [3, 4], have been used to restrain the propensity of fatigue initiation or growth by inducing compressive stress on the surface and fellow-surface regions to improve the fatigue performance of metallic materials. Compared with other surface treatment technologies, LSP has unique advantages that it could be performed contactless with component and without heat-affected zone.

The temperature and exposure time are the primary parameters for the thermal relaxation of residual stress. Masmoudi et al. [5] have studied the thermal relaxation of residual stress in shot peened Ni-based alloy IN100 as exposed to different temperatures (500–750 °C). During the initial period of exposure, the surface residual stress decreased rapidly. Cao et al. [6] also observed similar phenomena. Khadhraoui et al. [7] performed an experiment to investigate thermal stress relaxation in IN718 with different exposure times at 600 and 650 °C. Prevey et al. [1] studied the thermal stress relaxation of the compressive layer produced by LSP. Cai et al. [8] studied the residual compressive stress field of IN718 induced by shot peening and the relaxation behavior during aging, and the relaxation process was described by the Zener–Wert–Avrami function [9, 10].

In most cases [11], the residual stress relaxation of surface treated alloys is studied through experimental trials, which are expensive, time-consuming, and unreliable resulting from the factors arising from setting up the LSP process and residual stress measurements. Recently, the FE method has been used to study LSP-induced residual stress in titanium alloys [9], and the simulation results are well consistent with the experimental results. However, there is little FE analysis on thermal relaxation of residual stress having been performed. The purpose of this chapter is to study the residual stress distribution in GH4169 induced by LSP and the stress relaxation behaviors under thermal loading condition.

2.2.2 LSP Simulation

2.2.2.1 Thermal Relaxation

High-pressure shock waves are induced after laser having an impact on the absorption layer and constraint layer attached to the surface of components, which propagates into the material and causes plastic deformation resulting to residual stress field. In order to accurately simulate the LSP and the subsequent thermal relaxation process, the material constitutive model must accord with the properties of the material and the deformation of the FE model. During the LSP, material experiences extremely high strain rate reaching the order of 10^6 s^{-1}. In addition, the flow stress would reduce at elevated temperature, and the temperature effect is thought to be the primary reason causing the thermal relaxation of residual stress. A lot of material models have been developed to explain the effect of strain hardening, strain rate hardening, and thermal softening. These models include Johnson–Cook (JC) [9, 10, 12], Khan–Huang–Liang (KHL) [9], Cowper–Symonds [13], Zerilli–Armstrong (ZA) [14], and optimization of ZA. In this study, JC model is employed for that it is widely used for impact applications and is available in material model library in many commercial FEM codes, such as ANSYS/LSDYNA which is used in this study. Coupled structural/thermal implicit analysis is performed for thermal stress relaxation [9, 10]. JC model is given as

$$\sigma = [A + B(\varepsilon^p)^n][1 + C\ln(\varepsilon^{-p}/\varepsilon_0)][1 - T^{*m}] \tag{2.1}$$

where σ is the flow stress; ε^p is the effective plastic strain; ε^{-p} is the effective plastic strain rate, and ε_0 is reference strain rate; A, B, C, n, and m are experimentally determined constants. $T^* = (T - T_r)/(T_m - T_r)$, where T is the temperature in Kelvin, and T_r and T_m are room temperature and melting temperature, respectively.

2.2.2.2 Experimental Materials and Parameters

For the purpose of saving the memory of computer and shortening the computation time, only a quarter of models are created. The energy of laser is 8 J, the diameter of spot is 3 mm, and the pulse width is 10 ns. The FE model with 8-noded solid element is shown in Fig. 2.1, which has 178,596 nodes and 169,000 elements. As Ni-based alloy GH4169 and IN718 super alloy are similar materials, the original JC material model parameters for GH4169 (A = 900 MPa, B = 1200 MPa, C = 0.0092, n = 0.6, m = 1.27, $\varepsilon_0 = 1s^{-1}$) are taken from Zhong et al. [10]. After optimization, the JC material model with constants A = 860 MPa, B = 1100 MPa, C = 0.0082, n = 0.5, m = 1.05, and $\varepsilon_0 = 1s^{-1}$ is used for this study.

The pressure waveform of laser shock wave is similar to the laser wave profile tested by oscilloscope, according to Fabbro et al.'s findings [14, 16]. The studies have shown that the response time of laser inducing shock wave is about 3 times of the laser pulse width, or even longer. In this study, as the laser pulse width is 10 ns, the response time is set as 70 ns. The temporal pressure pulse profile is shown in Fig. 2.2b.

The residual stress from FE simulation is plotted in Fig. 2.3. Figure 2.3 shows the distributions of the residual stress with laser energy 6, 8, 12 and 15 J,

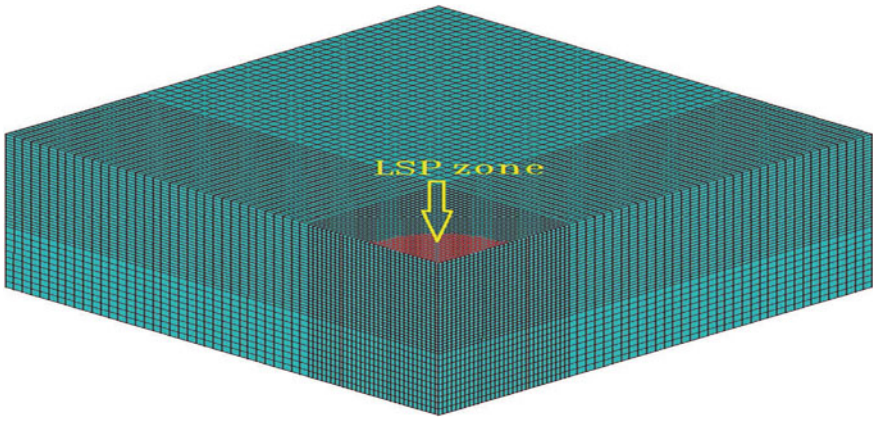

Fig. 2.1 FE meshes of 10, 10, and 5 mm for LSP and thermal relaxation analysis. Reprint from Ref. [15], Copyright 2014, with permission from Elsevier

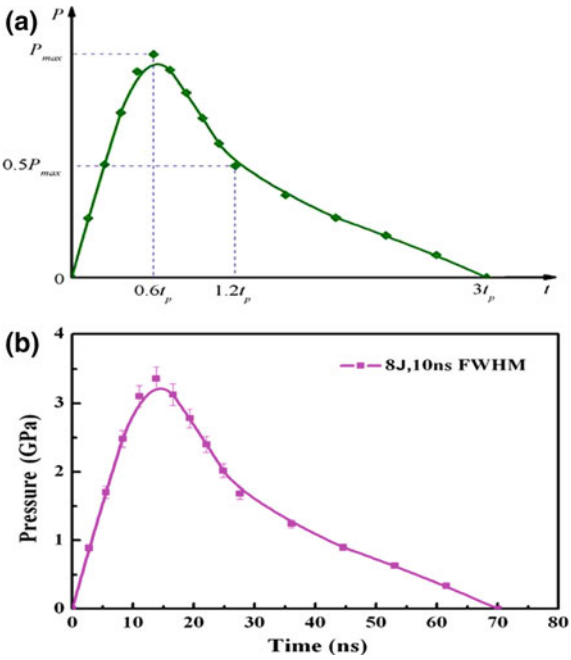

Fig. 2.2 **a** Amplitude curve of shock pressure; **b** Temporal pressure pulse profile. Reprint from Ref. [15], Copyright 2014, with permission from Elsevier

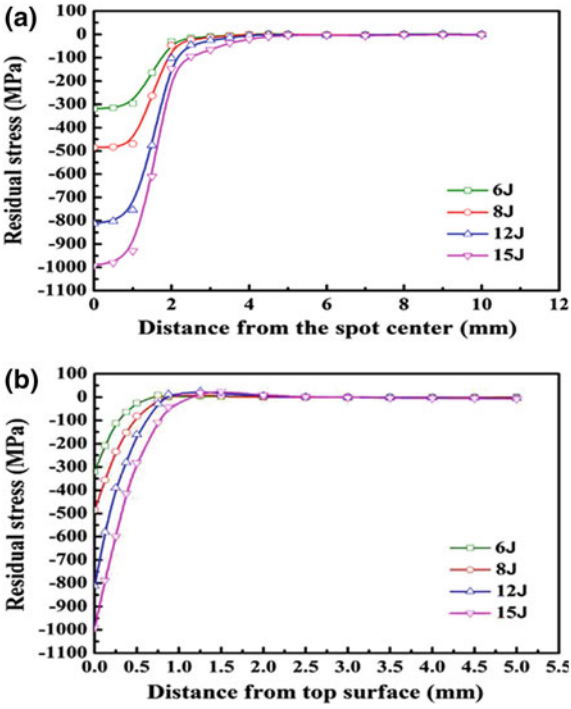

Fig. 2.3 Residual stress induced by LSP with 6, 8, 12 and 15 J. **a** Surface residual stress fields with single impacts; **b** Residual stress fields along with the depth with single impacts. Reprint from Ref. [15], Copyright 2014, with permission from Elsevier

respectively. It could be observed that the maximum compressive stress increases as the laser energy rises. And the same trend is shown in the depth of compression layer. A higher magnitude of stress is obtained for greater laser energy. The JC model has good agreement with experimental results, indicating the well consistency of the model [4].

2.2.3 Results and Discussion

2.2.3.1 Simulation of Thermal Relaxation of Residual Stress

The FE model for simulating the thermal relaxation of residual stress induced by LSP is the same as the one used in the LSP analysis. The mechanical loading is removed, and the thermal loading is applied at the top, bottom, and the both sides of the surface to simulate the thermal relaxation process. This process is simulated through a coupled thermal–structure analysis using ANSYS/LS-DYNA, with implicit algorithm for both thermal and structure analysis. The purely thermal loading condition is simulated by using a convection boundary condition $q = h(T - T_\infty)$, where q is heat flux across the boundary, h is heat transfer coefficient [100 W/(m^2 °C)], T_∞ is the imposed heating temperature, and T is the initial temperature of specimen. The initial temperature of the Ni-based alloy GH4169 specimen before applying thermal loading is set as the room temperature. The heat capacity of GH4169 is 481.4 J/(kg °C), and the thermal conductivity is 13.4 W/(m °C).

The residual stress induced by LSP with laser energy of 8 J and its relaxation as a function of exposure time at 500, 600 and 700 °C are shown in Fig. 2.4. The result reveals that only a little relaxation occurred at temperatures. It is expected that a greater degree of thermal relaxation would take place when the temperature becomes high enough to reduce the yield stress of GH4169. Another mechanism of thermal relaxation arises when the residual stress reaches sufficiently high values as to exceed the yield stress at the temperature of interest [10].

Figure 2.4a, b also shows that the maximal relaxation occurred at the zone of maximum residual stress. Stress relaxation mainly occurs in the initial exposure period, then the residual stress tends to stabilize at a longer exposure time, and eventually the relaxation essentially stops. The results are consistent with those studies [6, 17–19], which indicates a large portion of total relaxation of residual stress occurring in the initial period of exposure (normally between 3 min and 1 h) and following by a stabilization of stress. The effect of temperature on the thermal relaxation behavior is also showing in Fig. 2.4. The amplitude of the thermal relaxation increases with an increase in temperature. In addition, the effect of temperature is more significant at longer exposure time. Similar phenomenon could also be found in Zhong et al. [9, 10].

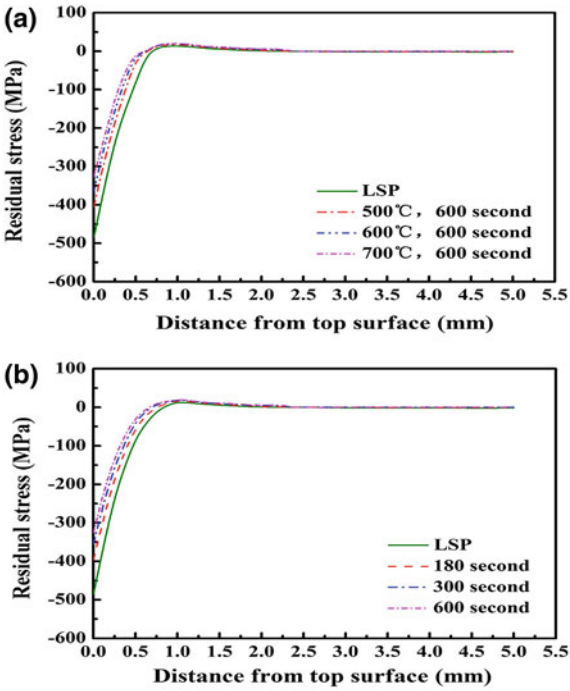

Fig. 2.4 The effect of temperature on the thermal relaxation behavior; **a** Thermal stress relaxation in GH4169 at different temperatures with a constant exposure time; **b** Thermal stress relaxation in GH4169 at different exposure time with a constant temperature. Reprint from Ref. [15], Copyright 2014, with permission from Elsevier

2.2.3.2 Analytical Model for Thermal Relaxation in GH4169

The residual stress is simulated with different exposure times at a constant high temperature and different high temperatures at a constant exposure time. The main work of this study focuses on the effect of temperature and exposure time on thermal stress relaxation.

A stress relaxation model by employing the Zener–Wert–Avrami function [9, 10, 20–22] was proposed to provide an analytical description of the thermal relaxation of residual stress,

$$\frac{\sigma^{\mathrm{RS}}}{\sigma_0^{\mathrm{RS}}} = \exp[-(At_a)^m] \tag{2.2}$$

where, σ_0^{RS} is the initial value of residual stress prior to apply thermal loading; σ^{RS} is the residual stress at a given time t_a at temperature T_a; m is a numerical parameter dependent on the dominant relaxation mechanism; and A is a function dependent on the material and temperature according to,

$$A = B\exp\left[-\frac{\Delta H}{KT_a}\right] \tag{2.3}$$

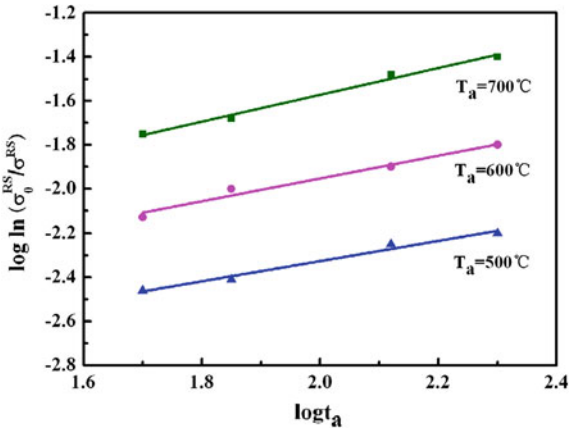

Fig. 2.5 Influence of heating temperature and exposure time on the thermal stress relaxation of GH4169. Reprint from Ref. [15], Copyright 2014, with permission from Elsevier

where B is a constant, K is the Boltzmann constant, and ΔH is the activation enthalpy for the relaxation process in the t_a–T_a range under consideration.

From Eq. (2.2), a plot of $\log \ln\left(\sigma_0^{RS}/\sigma^{RS}\right)$ versus $\log t_a$ at a given aging temperature T_a gives a straight line with slope m and intercept $m \log A$ shown in Fig. 2.5. The m value resulting from data fit at different temperatures gives a mean value of $m = 0.68$. The intercept value of these straight lines gives the value of A as a function of T_a, so that it is possible to estimate the activation enthalpy (ΔH) of the relaxation process for the LSP GH4169 referring to Eq. (2.3). The calculated value of ΔH is 3.02 eV, which is quite close to the value of 2.88 eV reported by Zhong et al. [10] for pure Ni using ion beam sputtering technique.

Dynamic recovery is the main relaxation mechanism during the stress relaxation between 400 and 500 °C in LSP 6061-T651 aluminum alloy [22]. Essentially, dynamic recovery is the result of the dislocation slip, the dislocation climb, and the reducing of dislocation density [22]. We conjecture that it is the creep-like mechanism involving rearrangement and annihilation of dislocations by climbing that causes the thermal relaxation. After the initial stress relaxation, subsequent stress relaxation becomes considerably lower, as the stress has dropped below the creep strength of the alloy at temperatures, and therefore, the driving force is reduced. However, further metallographic structure studies are needed to verify this, which is beyond the scope and purpose of this paper.

2.2.4 Summary

The residual stress in the Ni-based alloy GH4169 induced by LSP and the associated thermal relaxation behaviors were analyzed based on a three-dimensional nonlinear FE model.

At higher temperatures, the maximum thermal relaxation occurs at the depth of the maximum compressive residual stress. A significant decrease of the residual stress is observed at the initial exposure period followed by a stabilization of the stress relaxation at the next long exposure times.

The degree of thermal relaxation increases as the temperature rises, and the effect of temperature is more significant at longer exposure times.

Further work should be carried out to study the material model and methodology in overlap case using the single shot. Furthermore, to further study the effect of plastic deformation, the thermal relaxation behavior of doubly shocked and triply shocked specimens at a constant temperature will be simulated.

2.3 Comparison of the Simulation and Experimental Fatigue Crack Behaviors in the Nanoseconds Laser Shocked Aluminum Alloy

Abstract This chapter was performed to compare the simulation and experimental results of the fatigue crack growth rates and behaviors of the 7050-T7451 aluminum alloy by nanoseconds LSP. Forman–Newman–deKoning (FNK) model embedded in the Franc2D/L software was utilized to predict fatigue crack growth rate, which was conducted to weigh the stress intensity factor (SIF) changing on the surface cracks. LSP induced high compressive residual stresses that served to enhance fatigue properties by improving the resistance against fatigue crack initiation and propagation. The circulating times of crack growth obtained from the simulation and experimental values indicated a slower fatigue crack growth rate after LSP. The relationships between the elastic–plastic material crack growth rates and the SIF changing after LSP are resolved.

2.3.1 Introduction

Fracture mechanics typically offers a reliable foundation for the description of the fatigue growth of cracks. It is well known that residual stress plays a crucial role in fatigue crack growth behavior [23–26]. LSP is a competitive technology as a method of imparting compressive residual stresses into the metal surface to improve fatigue and corrosion properties [27, 28].

The research on stress shock wave on cracks has made great progress in aspects of theoretical and numerical simulations. A numerical model for predicting the depth of plastic deformation and resulting residual compressive stress at the surface has been completed by ArifAbulFazal [29]. The plastic behavior near the tip of stationary crack in engineering materials has been intensively studied by using classical plasticity theory based on the von Mises yield criterion [30] and the

associative flow rule [31]. Ray and Patanker [32] derived the crack closure models on the crack opening stress by FE computations. Then, the theoretical analysis work which confirmed the effect of the compressive residual stresses generated by LSP on the SIF has been put forward [33, 34], showing the influence of compressive stress on the 3D non-through hole-edge crack's SIF after LSP.

However, the relationships between the fatigue crack growth rates and the surface SIF changing after LSP have never been reported in literature to the authors' best knowledge. With respect to the continuity information between this study and the available literature, we aim to characterize the effects of residual stress on fatigue crack propagation under variable laser shock amplitude loading. Moreover, we will also discuss simulation results on the dynamic response of cracks under the actions of various shock loads, and we use the crack growth function of Franc2D/L to present the curve of the surface SIF changing under residual stress loads. Further studies on the issue of optimal fracture with the action of stress pulses will be summarized in our next study.

2.3.2 Simulation Methods

2.3.2.1 Fracture Analysis Software

Franc2D/L is the professional fracture analysis software based on FE analysis and developed by Cornell Fracture Group. Franc2D/L initialized cracks and predetermined the initiation spots of cracks. Then the software judged the cracks growing direction so as to perform numerical simulation of crack growth and obtain results automatically. Figure 2.6 shows the sample of the singularized element growing along with the crack tip. The crack tip has been modeled with a rosette of eight quarter-point collapsed elements. The propagation of the crack is divided into many steps, and in every step, the crack is let to extend to a certain amount. The first propagation step is set to 0.5 mm, while the following crack propagation steps are 1 mm each. After each step, Franc2D/L remeshes the region in front of the crack tip and calculates the SIF and the kink angle. The crack propagation direction is determined according to the maximum hoop stress criterion (MHSC) [35, 36], and K_{I} and K_{II} are determined at every step.

2.3.2.2 Crack Growth Model

The FNK model was used to determine the crack growth rate, which could account for retardation near threshold, acceleration near fast fracture, and the crack closure. This method is given as [38],

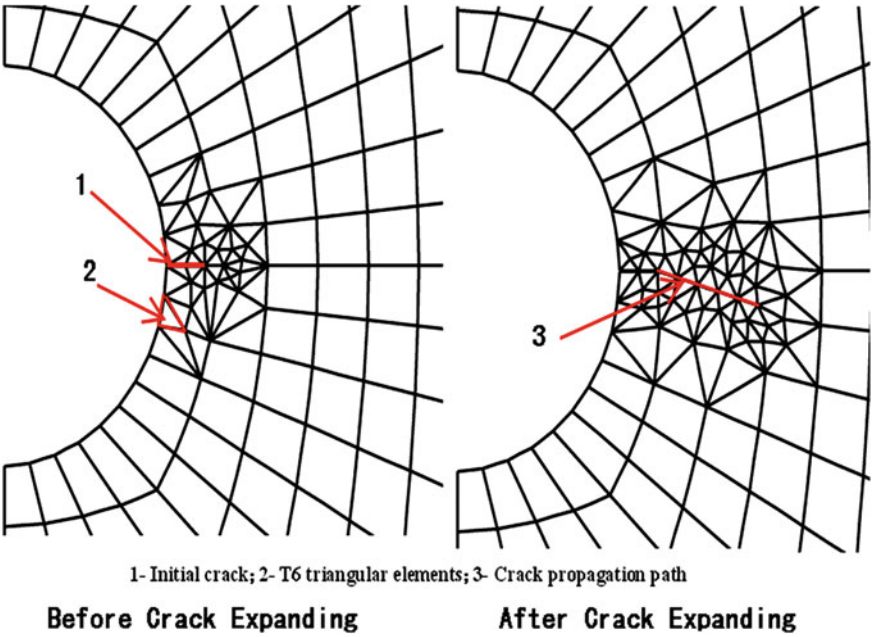

Fig. 2.6 Sample of the singularized element growing along with the crack tip of 7050-T7451 aluminum alloy by Franc2D/L. Reprint from Ref. [37], Copyright 2011, with permission from Elsevier

$$\frac{\mathrm{d}a}{\mathrm{d}N} = \frac{C(1-f)^n \Delta K^n \left[1 - \frac{\Delta K_{th}}{\Delta K}\right]^p}{(1-R)^n \left[1 - \frac{\Delta K}{(1-R)K_C}\right]}$$

where C, , n, and p are empirically derived by curve fitting test data [39, 40], R is the stress ratio, f is the function of maximum applied stress and strain constraint factor, ΔK_{th} is the threshold value that is a function of R, K_C is a function of fracture toughness and specimen thickness, and ΔK is the range of the SIF.

The analysis results of the cracked configuration are used to compute the Mode I-type SIF which are used in a closed-form expression, and this expression determines the direction from the maximum circumferential stress around the crack tip. Propagation angle is also displayed to give the option of propagating the crack by an incremental distance along crack line during crack propagation.

2.3.3 Experimental Methods

2.3.3.1 Sample Preparation

7050-T7451 aluminum alloy was made into single-edged notched tensile (SENT) samples, as shown in Fig. 2.7. The alloy's chemical composition and mechanical properties are shown in Tables 2.1 and 2.2 separately.

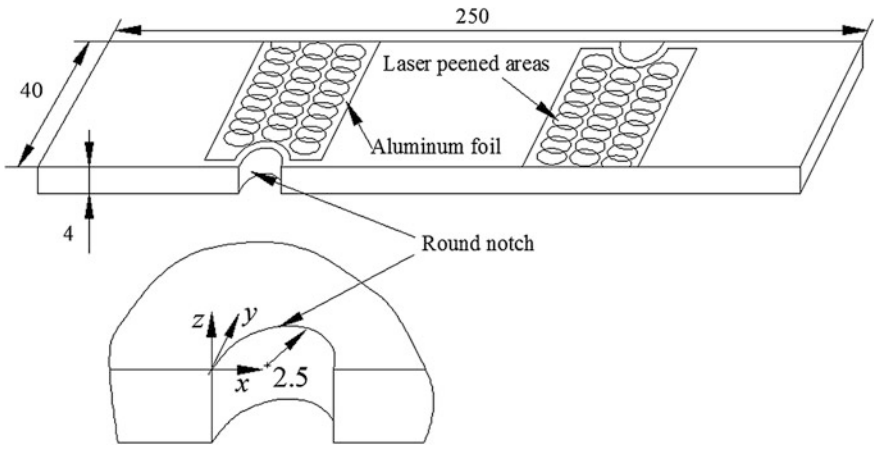

Fig. 2.7 Dimensions of the 7050-T7451 SENT specimen and laser shock processing route. Reprint from Ref. [37], Copyright 2011, with permission from Elsevier

Table 2.1 7050-T7451 chemical composition

Trademark	Si	Fe	Cu	Mn	Mg	Cr	Zr	Zn	Ti	Al
7050	≤0.12	≤0.15	2.0–2.6	≤0.10	1.9–2.6	≤0.04	0.08–0.15	5.7-6.7	≤0.06	Rest

Table 2.2 7050-T7451 mechanical properties

Trade mark	Supply condition	Thickness (Mm)	Sampling direct	No less than		
				Tensile stress (MPa)	Non-proportional extension strength $\sigma_{0.2}$ (MPa)	Elongation after break (%)
7050	T7451	60–76	L	503	434	9
			LT	503	434	8
			ST	469	407	3
		>76–102	L	496	427	9
			LT	496	427	6
			ST	469	400	3

Notes L is portrait line section; LT is landscape orientation line section; ST is thickness

2.3.3.2 Experimental Parameters

LSP was performed by high power Nd:glass laser implements to investigate the effect of the processing parameters on the residual stress distribution. Laser beam wavelength was 1.054 μm, pulse duration and power density were 20 ns and 2.91 GW/cm^2, respectively, and laser beam spot size was maintained at 8 mm. LSP experiment was conducted with a confined plasma configuration. A thin aluminum foil adhesive tape was used as the energy absorbing layer, and a water-tamping layer was used as the plasma confinement layer. The region with a hole was laser shocked, and nearly pure mechanical effects were induced, as shown in Fig. 2.8. The distributions of residual stress along the radial direction at the surface direction and depth direction were determined by using the X-350A X-ray diffraction technique. MTS880 material testing system was adopted for fatigue experiment in which tensile stress fatigue was adopted with load control. The stress ratio R was 0.1, alternating frequency was 20 Hz, σ_{max} was 460 Mpa, and the loading wave was sine wave.

2.3.4 Results and Discussions

2.3.4.1 Residual Stress Distributions

The laser-generated shock wave affects both the surface and side surface during its propagation. Residual stress distributions as a function of surface distance and depth are shown in Fig. 2.9. The contours of radial stress shown in Fig. 2.9a

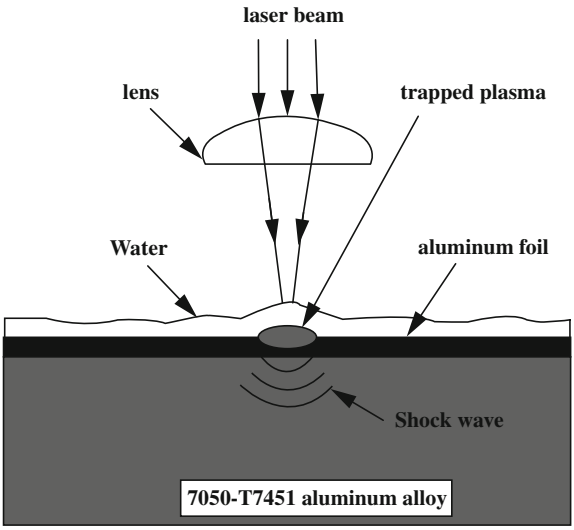

Fig. 2.8 Schematic of the laser shock processing principle. Reprint from Ref. [37], Copyright 2011, with permission from Elsevier

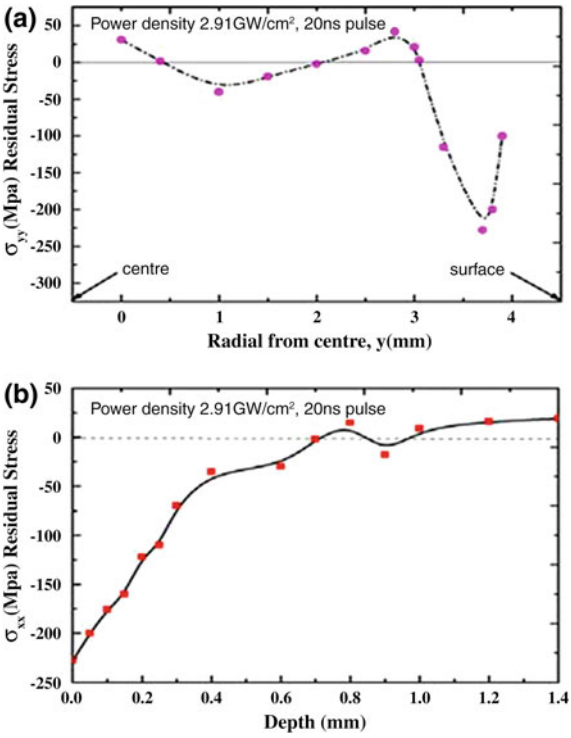

Fig. 2.9 Diagram of surface residual stresses of the 7050-T7451 aluminum alloy tensile SENT specimen induced by laser shock processing. **a** σ_{yy} in-surface and **b** σ_{xx} in-depth. Reprint from Ref. [37], Copyright 2011, with permission from Elsevier

indicate that it is compressive with a maximum of 227 MPa at 20 ns with a 2.91 GW/cm^2 power density, and the residual radial stress distribution over the depth of the substrate is given as Fig. 2.9b. It is observed that the residual stresses are compressive. The maximum residual stress occurs at a depth of about 0.09 mm, and it is evident from the residual displacement at 20 ns that the axial displacement is confined to the beam impact region with a maximum of 1.0 mm. This pattern agrees well with the results reported in the literature [41].

2.3.4.2 Microscopic Analysis of Macroscopic Fracture

The laser-induced shock waves have a very high intensity which could reach several or even dozens of GPa, while their pulse widths are dozens of nanoseconds generally. Therefore, solid substances will generate some ultra-high strain rates, which are as much as 10^6–10^7 s^{-1} under the action of laser shock waves. Alloy materials usually have some special mechanical and physical characteristics under so high strain rates; their structures may generate dislocation, grains, and twins. And surface roughness, deformation, residual stress, and hardness of the material surface will be changed greatly [20, 21].

Typical macroscopic fracture morphology of the non-treated specimen (tested at 300 MPa) is shown in Fig. 2.10. Figure 2.10a shows the overall macroscopic appearance of the fracture, where internal longitudinal crack is seen in the central area of the specimen, and Fig. 2.10b shows the detail of the longitudinal crack. Several of these longitudinal cracks were formed near the central area of the specimen. As expected, the fatigue striation distance increased as the crack length increasing. The fatigue cracks are initiated from these cracks and grew until failure.

However, fatigue striation spacing in the LSP specimen (tested at 300 MPa) was narrower than those observed on the non-treated one, as shown in Fig. 2.11a, b. The distance between fatigue striations was narrow, and the number of striations was very large in the laser shock zones, which indicated that the crack expansion distance was small, and it means that LSP had an inhibition effect on the material fatigue crack initiation and expansions. The reduction in striation spacing indicated a slower

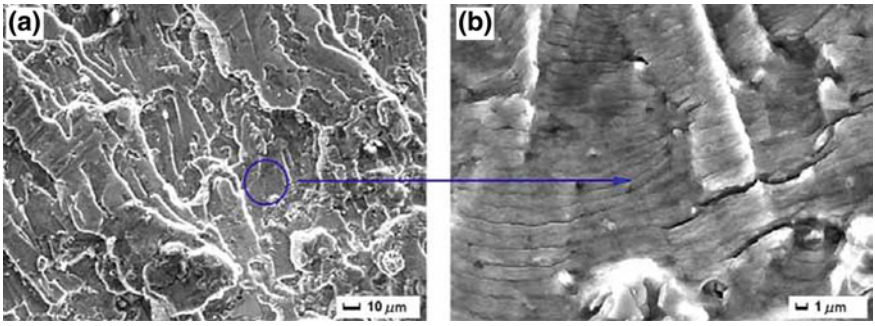

Fig. 2.10 Fractured surface of the non-LSP-treated 7050-T7451 aluminum alloy at an applied stress of 300 MPa, $R = 0.1$. **a** Macroscopic fracture appearance of a non-LSP-treated specimen and **b** detail of an internal crack across the center of the specimen. Reprint from Ref. [37], Copyright 2011, with permission from Elsevier

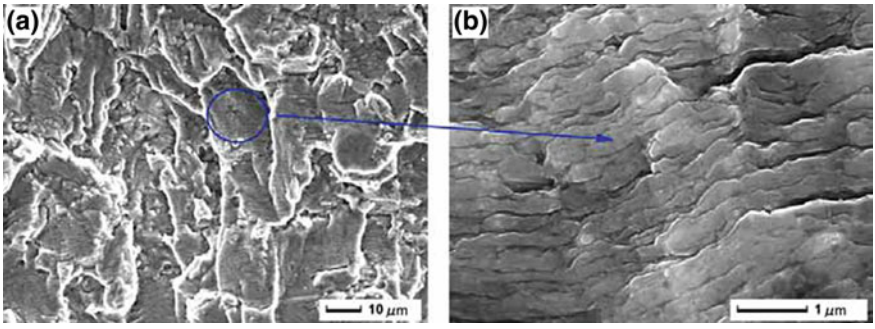

Fig. 2.11 Fractured surface of the LSP-treated 7050-T7451 aluminum alloy at an applied stress of 300 MPa, $R = 0.1$. **a** Macroscopic fracture appearance of a LSP-treated specimen and **b** detail of an internal crack across the center of the specimen. Reprint from Ref. [37], Copyright 2011, with permission from Elsevier

fatigue crack growth rates, which could be attributed to the compressive residual stress induced by LSP. As a result, the effective SIF that controls the fatigue crack growth in the LSP specimen is lower than that of the non-LSP case. The scatter in the spacing could be attributed primarily to the fact that striation formation is a highly localized event. The striation spacing is also dependent on both the SIF and metallurgical factors such as variations in the grain orientation [42].

2.3.4.3 Numerical Calculation of I-Type Cracks

Franc2D/L was applied in the stable-growth numerical calculation of I-type cracks on 7050-T7451 aluminum alloy. The elastic modulus E was defined as 71 GPa, Poisson ratio ν was 0.345, and experimental load value DF was defined as 20 kN. After each step of crack growth, Franc2D/L calculated the SIF of each crack tip by using J-integral method to decide the next growing step of each crack. The crack length shows a monotonically increasing trend (Fig. 2.12). Nevertheless, a bifurcation will take place due to the nucleation of a vertical penny-shaped crack beneath the contact area as soon as the load is sufficiently increased. Therefore, the exact simulation of the propagation pattern requires a three-dimensional analysis, which is beyond the capability of the code unfortunately. The crack propagates following a sub-vertical pattern, and no bifurcations are observed. It is worth noting that the length is the only characteristic length of this structural scheme. Therefore, it is useful to plot the diagram of the non-dimensional SIF as a function of the crack length so as to emphasize the scale-invariant aspects of the problem.

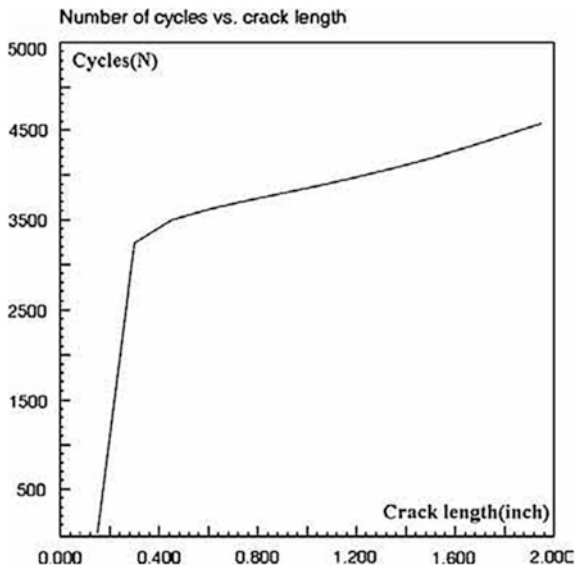

Fig. 2.12 The relationship of the crack length and fatigue cycles along with the surface crack expanding curve with Franc2D/L. Reprint from Ref. [37], Copyright 2011, with permission from Elsevier

2.3.4.4 Improvement in Fatigue Life by LSP

The growth data of fatigue cracks were obtained based on the experimental data of the cracked sample by MTS880 fatigue experiment machine. The fatigue lives of specimens treated by LSP and un-treated specimens at the maximum applied stress of 460 Mpa are shown in Fig. 2.13. In an earlier study [43] of LSP-treated 7050-T7451 specimens, the expected large extension of fatigue life was not achieved. While in this study, LSP resulted in an improvement of 29 and 47 % in the number of fatigue cycles, after one and two laser shock layers (100 and 200 % coverage), respectively. The mean value in fatigue life of the specimens treated by LSP was higher than that of those untreated under the same maximum applied stress. This improvement is explained by the greater depth of the residual compressive stress fields induced by laser processing as comparing with non-treated sample. Further examination of these preexisting internal cracks was carried out to find an explanation for the fatigue lives of LSP specimens longer than expected. The number of fatigue cycles was compared to the experimental results when the crack length growing to 25 mm (1 in.). The computer-simulated fatigue circulating time was 38,509, while the fatigue experiment machine test value was 40,025. In the FNK model, numerical results are fairly good regarding the fatigue limit while they are conservative above it. This can be further demonstrated by plotting K_{res}, the residual value of K calculated from the residual stress field, as a function of distance from the leading edge. It is evident that Franc2D/L model provides good predictions for the crack growth circulating times.

A path following the initial crack growth is defined to make clear the residual stress field SIF. Figure 2.14 shows the Mode I-type SIF history for a single trace along the crack surface. The SIF varies along the crack front; thus, the SIF history and the predicted fatigue life would vary depending on the chosen path. Using the FNK fatigue crack growth model and the material parameters from Table 2.2, the

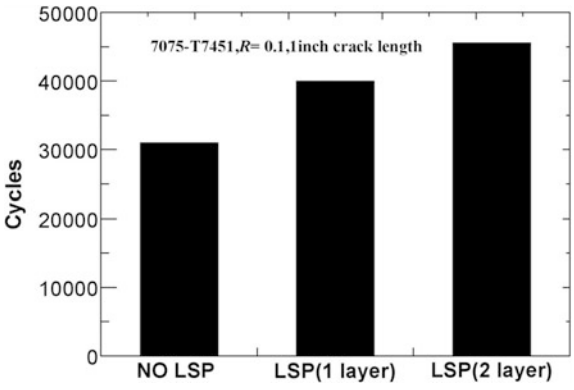

Fig. 2.13 Comparison of the fatigue crack expanding cycles of the 7050-T7451 aluminum alloy at the rate of $R = 0.1$ before and after LSP. Reprint from Ref. [37], Copyright 2011, with permission from Elsevier

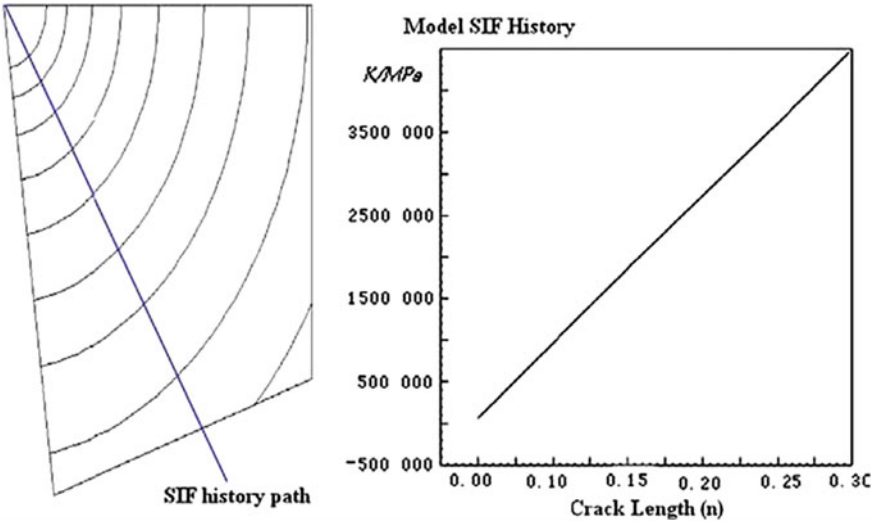

Fig. 2.14 Schematic of mode I-type SIF changing along the crack surface. Reprint from Ref. [37], Copyright 2011, with permission from Elsevier

number of predicted fatigue life starting from an initial surface crack is about 9200 cycles, as shown in Fig. 2.15. Due to the high levels of compressive residual stresses at the surface of the specimen, and analogous to the effect of LSP on crack growth, the cracks show considerable retardation upon reaching the treated region.

However, the curve of the crack length and the number of load cycle measurements did not show any considerable retardation of the fatigue cracks. This is believed to be due to the tensile core in the material that arises as a by-product of LSP. This tensile region is essential for the internal balance of forces in the unloaded component. Mahorter et al. [44] reported that the low cycle fatigue (LCF)

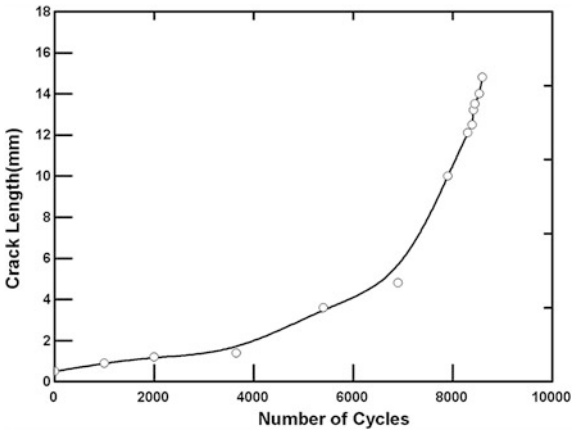

Fig. 2.15 Prediction of the fatigue life along with the crack length on 7050-T7451samples with Franc2D/L. Reprint from Ref. [37], Copyright 2011, with permission from Elsevier

life of the disk ended when the crack in the bolt-hole reached 1/32 in. (0.79 mm), this corresponded to the life which was expressed as a 1/1000 probability of failure. The analyses presented here provide an estimate of remaining life once the LCF life is reached. Additional simulations could be performed to estimate the LCF life as well [36], but this is beyond the scope and purpose of this paper. It appears that the deflection point in the curve is barely noticeable, and hence, a sensitive measuring system requires to be detected.

2.3.5 Summary

The relationship of the 7050-T7451 aluminum alloy fatigue crack growth behaviors and surface SIF changing has been developed after nanoseconds LSP.

1. Compressive residual stress generated by LSP in crack surface reduces the tensile stress level in alternating load and decreases the effective driving force of fatigue crack growth. The reduction in striation spacing indicates a slower fatigue crack growth rates which would be attributed to the compressive residual stress (about to 250 Mpa) induced by LSP.
2. The effective SIF that controls the fatigue crack growth in the LSP specimen is lower than that of the non-LSP case. The more intense the residual stress produced by laser shock is, the smaller the effective SIF of crack surface becomes, resulting in the lower crack growing speeds.
3. FE analyses were carried out to determine the effective SIF at the crack tip. Reasonably, good agreements have been obtained from both the simulation and experiment results. The number of cycles to failure predicted numerically is lower than the experimental one. This difference is attributed mainly to an early stage of shear-dominated propagation that cannot be accounted for in the numerical model. All these illustrate the flexibility and interaction of Franc2D/L in simulating the process of crack growth with the residual stresses and SIF changing after LSP.

References

1. Prevey P et al (1998) Thermal residual stress relaxation and distortion in surface enhanced gas turbine engine components. In: Proceedings of the 17th heat treating society conference and exposition and the 1st international induction heat treating symposium. ASM Materials, Park, OH: pp 3–12
2. Paul SP et al (2001) The effect of low plasticity burnishing (LPB) on the HCF performance and FOD resistance of Ti-6Al-4 V. In: Proceedings of the 6th national turbine engine high cycle fatigue (HCF) conference, Jacksonville
3. Charles SM et al (2002) Laser shock processing and its effects on microstructure and properties of metal alloys: a review. Int J Fatigue 24:1021–1036

4. Amarchinta HK et al (2009) Material model validation for laser shock peening process simulation.Modell Simul Mater Sci Eng. http://iopscience.iop.org. Accessed 21 Jan 2013
5. Masmoudi N et al (1989) Influence of temperature and time on the stress relaxation process of shot peened IN 100 superalloys. Mater Tech (Paris) 77:29–36
6. Cao W et al (1994) Thermomechanical relaxation of residual stress in shot peened nickel base superalloy. Mater Sci Technol 10:947–954
7. Khadhraoui M et al (1997) Experimental investigations and modelling of relaxation behaviour of shot peening residual stresses at high temperature for nickel base superalloys. Mater Sci Technol 13:360–367
8. Cai DY et al. (2006). Precipitation and residual stress relaxation kinetics in shot-peened Inconel 718. J Mater Eng Perform 15(5):614–617
9. Zhong Z et al (2012) Thermal relaxation of residual stress in laser shock peened Ti-6Al-4 V alloy. Surf Coating Technol 206:4619–4627
10. Zhong Z et al (2011) A finite element study of thermal relaxation of residual stress in laser shock peened IN718 superalloy. Int J Impact Eng 38:590–596
11. Dennis JB et al (2009) A coupled creep plasticity model for residual stress relaxation of a shot peened Nickel-base superalloy. Mater Technol 131:75–79
12. Jeffrey JD et al (2009) Effects of material microstructure on blunt projectile penetration of a nickel-based super alloy. Int J Impact Eng 36:1027–1043
13. Marco DS et al (2003) Low and high velocity impact on Inconel 718 casting plates: ballistic limit and numerical correlation. Int J Impact Eng 28:849–876
14. Fabbro R, Pournier J, Ballard P (1990) Physical study of laser-produced plasma in confined geometry. J Appl Phys 68:775–784
15. Ren XD et al (2013) A finite element analysis of thermal relaxation of residual stress in laser shock processing Ni-based alloy GH4169. Mater Des 54(2014):708–711
16. Peyre P et al (1996) Laser shock processing of aluminium alloys. Application to high cycle fatigue behavior. Mater Sci Eng A 210:102–113
17. Evans A et al (2005) Relaxation of residual stress in shot peened Udimet 720 Li under high temperature isothermal fatigue. Int J Fatigue 27:1530–1534
18. Feng BX et al (2009) Residual stress field and thermal relaxation behavior of shot-peened TC4-DT titanium alloy. Mater Sci Eng A 512:105–108
19. Aghdam AB et al (2010) An FE analysis for assessing the effect of short-term exposure to elevated temperature on residual stresses around cold expanded fastener holes in aluminum alloy 7075-T6. Mater Des 31:500–507
20. Juijerm P, Altenberger I (2006) Residual stress relaxation of deep-rolled Al-Mg-Si-Cu alloy during cyclic loading at elevated temperatures. Scripta Mater 55:1111–1114
21. Xie LC et al (2011) Thermal relaxation of residual stresses in shot peened surface layer of (TiB + TiC)/Ti-6Al-4 V composite at elevated temperatures. Mater Sci Eng A 528:6478–6483
22. Ren XD et al (2013) Metallographic structure evolution of 6061-T651 aluminum alloy processed by laser shock peening: effect of tempering at the elevated temperatures. Surf Coat Technol 221:111–117
23. Almer JD et al (2000) The effects of residual macrostresses and microstresses on fatigue crack initiation. Mater Sci Eng A 284:268–279
24. Genel K et al (2000) Effect of ion nitriding on fatigue behaviour of AISI 4140 steel. Mater Sci Eng A 279:207–216
25. Berger MC, Gregory JK (1999) Residual stress relaxation in shot peened Timetal 21s. Mater Sci Eng A 263:200–204
26. Heinz A et al (2000) Recent development in aluminum alloys for aerospace applications. Mater Sci Eng A 280:102–107
27. Warren AW et al (2008) Massive parallel laser shock peening: simulation, analysis, and validation. Int J Fatigue 30:188–197
28. Caslaru R et al (2009) Fabrication and characterization of micro dent array produced by laser shock peening on aluminum surfaces. Trans NAMRI/SME 37:159–166

29. ArifAbulFazal M (2003) Numerical prediction of plastic deformation and residual stresses induced by laser shock processing. J Mater Process Technol 136:120–138
30. Ramsamooj DV (2003) Analytical prediction of short to long fatigue crack growth rate using small and large-scale yielding fracture mechanics. J Fatigue 25(9–11):923–933
31. Edgar HK (1998) Some aspects of fracture mechanics research during the last 25 years. Steel Res 69:206–213
32. Ray A, Patanker P (2001) Fatigue crack growth under variable amplitude loading: part I - model formulation in state space setting. Appl Math Modell 25:979–994
33. Ren XD et al (2009) Influence of compressive stress on stress intensity factor of hole-edge crack by high strain rate laser shock processing. Mater Des 30:3512–3517
34. Zhang YK et al (2009) Investigation of the stress intensity factor changing on the hole crack subject to laser shock processing. Mater Des 30:2769–2773
35. Carpinteri A, Pugno N (2006) Cracks and re-entrant corners in functionally graded materials. Eng Fract Mech 73:1279–1291
36. Barlow KW, Chandra R (2005) Fatigue crack propagation simulation in an aircraft engine fan blade attachment. Int J Fatigue 27:1661–1668
37. Ren XD et al (2011) Comparison of the simulation and experimental fatigue crack behaviors in the nanoseconds laser shocked aluminum alloy. Mater Des 32(2011):1138–1143
38. Qian J, Fatemi A (1996) Mixed mode fatigue crack growth: a literature survey. Eng Fract Mech 55(6):969–990
39. Forman RG et al (1994) Fatigue crack growth computer program NASA/FLAGRO version 2.0. Johnson Space Center, Houston (Texas): Rpt. # JSC-22267A
40. Newman JC Jr (1984) A crack opening stress equation for fatigue crack growth. Int J Fract 24: R131–R135
41. Gomez-Rosas G et al (2010) Laser shock processing of 6061-T6 Al alloy with 1064 nm and 532 nm wavelengths. Appl Surf Sci 256:5828–5831
42. Hatamleh Omar et al (2007) Laser and shot peening effects on fatigue crack growth in friction stir welded 7075-T7351 aluminum alloy joints. Int J Fatigue 29:421–434
43. Liu Q et al (2002) Internal cracking during surface treatment of 7050-T74 aluminium alloy using laser shock peening. Int Conf Struct Integrity Fract 25–28:177–182
44. Mahorter R et al (1985) Life prediction methodology for aircraft gas turbine engine disks. In: AIAA/SAE/ASME/ASEE 21st joint propulsion conference, Monterey, CA, pp 1–6
45. Sadananda K, Vasudevan AK (2005) Fatigue crack growth behavior of titanium alloys. Int J Fatigue 27:1255–1266

http://www.springer.com/978-3-662-46443-4

Laser Shocking Nano-Crystallization and
High-Temperature Modification Technology
Ren, X.
2015, XIII, 131 p. 86 illus., Hardcover
ISBN: 978-3-662-46443-4